

Vortex Beam Generation in Microwave Band

Ahmad Alamayreh and Nidal Qasem*

Abstract—This paper describes a theoretical characterization of a Transverse Electric (TE)-polarized vortex beam antenna in the microwave range. The main body of the antenna consists of a cylindrical waveguide that is excited by a traveling-wave current ring feeder. A new design of the feeder is proposed. Closed-form formulas are obtained for the fields and the antenna input impedance following a conventional derivation based on the electric vector potential. A detailed dispersion analysis is used for accurate evaluation of the relevant spectrum and propagation properties. The effectiveness of the theoretical derivations is validated via full-wave numerical simulations.

1. INTRODUCTION

Spin angular momentum of light was discovered [1] and experimentally detected [2] a while before realizing [3] that light also possesses an Orbital Angular Momentum (OAM). OAM beams have been applied in a variety of areas in optics [4]. OAM orders form a complete, infinite-dimensional basis, which is promising for better utilization of the communications spectral. Not surprisingly, OAM carrying waves have fast found their way to radio and microwave applications. Indeed, the first radio OAM simulation was carried out [5] via a multi-feed circular antenna array. This stimulated a large research effort for generating OAM carrying waves. Some approaches were inspired by works in optics as the spiral plate feeder in [6]. Other approaches took another turn as the circular patch antenna approach in [7], the horn antenna in [8], and the circular leaky-wave antenna in [9], to name just a few.

OAM carrying waves exhibit helical phase-fronts, or vortices. This owns to the azimuthal dependence of the spatial phase distribution ($e^{jq\theta}$) of these waves, where q is the OAM order ($q = 0, \pm 1, \pm 2, \dots$), and θ is the azimuthal angle. The intensity cross-section of these waves is radially symmetric with no on-axis intensity. The field amplitude changes in the transverse direction as a q -th order Bessel function of first kind $J_q(\eta\rho)$, where ρ is the radial position in cylindrical coordinates. η is the transverse wavenumber which is related to the longitudinal wavenumber \mathcal{L} and the propagation wavenumber K by the separation relation $K^2 = \eta^2 + \mathcal{L}^2$. In free space, K is distinguished by the notation K_o .

Transverse Magnetic (TM)-polarized Bessel beam is generated in [10] by means of a cylindrical waveguide with a capacitive aperture sheet. Generation of Transverse Electric (TE)-polarized beams is addressed in [11] using an inductive aperture sheet. In addition to supporting the desired field polarization the aperture sheet can be controlled to influence the beam width and the bandwidth [12].

We propose generating TE-polarized OAM carrying waves by exciting a traveling-wave current in a two backed ring structure. The rings are concentric and closely placed. By appropriate selection of the rings' radii and the angular separation of the ports on the rings a traveling wave carrying OAM is produced. Generating traveling waves is considered from a mathematical perspective in [13]. A patch antenna-based design for generating traveling-waves is investigated in [14]. The antenna is formed from a conducting disc laying over a substrate and a ground plate. In another design [15], the traveling-wave

Received 20 August 2020, Accepted 26 October 2020, Scheduled 26 November 2020

* Corresponding author: Nidal Qasem (ne.qasem@ammanu.edu.jo).

The authors are with the Electronics and Communications Engineering Department, Al-Ahliyya Amman University, Amman, Jordan.

is radiated from a circular slit in the surface of a two-port excited resonator. In [16], the traveling-wave is produced using a circular waveguide by exciting two TE modes with 90° phase separation between them. The designs considered so far do not easily manipulate multimode OAM generation which is of great utility in multimode-MIMO systems [17, 18] and beam-forming [19]. Using the proposed design, two or more pairs of rings with different radii can be concentrically placed in the same plane to produce a superposition of multi OAM orders. Upon placing the basic two-ring structure in a cylindrical waveguide with an open end the radiation can be focused and directed. Focusing the radiation is of special importance at large OAM orders where beam divergence is notable [20]. Furthermore, among the parameters of the structure the axial location of the ring inside the waveguide can be controlled to achieve maximum power-matching with the coaxial feeder. The additional structure, however, could alter the spectrum characteristics of the ring radiator through shifting the main resonance and creating side-resonances. To analyze the complex spectrum a model including the different parameters of the vortex beam launcher is derived. This model is used along with dispersion analysis in an attempt to understand the changes in the spectrum when some design parameters are changed, such as the waveguide size and the location of the excitation rings inside the waveguide.

Mode-matching analysis method is used in [21] for investigating the resonance behavior. In this paper, the well-known transverse dispersion analysis is used for this purpose which leads to simple analysis and great accuracy. To model the system, the fields inside the waveguide are formulated to match the required excitation and boundary conditions. The overall input impedance spectrum of the design is then obtained and compared against full-wave numerical simulations.

Throughout this paper, a time-dependent term $e^{j\omega t}$ is implicitly assumed, where ω is the radial frequency. The next section includes a general overview of the design model. This is followed by derivation of the field expression in Section 3 and the model input impedance in Section 4. The dispersion relation is then obtained in Section 5. The relation between the dispersion curves and the impedance spectrum is explained next in Section 6. Numerical results and the comparisons between derived formulas and those obtained via CST simulations are shown in Section 7. Finally, conclusions are drawn in Section 8.

2. SYSTEM MODEL

Using thin conducting rings we aim at exciting a current-traveling wave in the form $I_o e^{j\frac{2\pi}{\lambda}\theta d}$, where λ is the wavelength, and d is the ring radius. This waveform will have the spatial phase characteristics of a q -th order OAM wave ($e^{jq\theta}$) when the ring circumference is set equal to $q\lambda$. In principle, a traveling wave can be generated as a superposition of two standing waves having 90° electrical difference. The sources of the standing waves are connected at appropriate points on the ring circumference in a way that each source lays in the null of the other source. These locations are obviously related to the OAM order of the generated wave. For instance, angle separation of 30° is required between the sources for an OAM wave of order 3 while 22.5° is needed when the OAM order is 4. This is implemented in the structure appearing in Fig. 1. Two rings are used to direct the path of the excitation wave. The average radius of the rings (d) is determined according to the OAM order. The inner ring has a slightly smaller radius and is used as the ground. It is found through numerical simulations that a large separation of the rings could create distortion in the standing wave pattern. On the other hand, a minimum distance should be provided between the rings to make it possible for physically placing the ports.

To focus and direct the radiation the rings are placed in the waveguide structure shown in Fig. 2(a). The design consists of a cylindrical waveguide of radius a and length h with the axis defined along the z -direction. One of the waveguide ends is terminated by a Perfect Electric Conductor (PEC) and the other is left open. The rings are placed coaxially inside the waveguide at a distance z_a from the PEC. Feeding the rings from outside the waveguide is shown in Fig. 2(b) for a case of 4th order OAM. The feeding line is branched and connected at two points to the outer ring. A difference of quarter wavelength between the feeding line branches will satisfy the required 90° electrical phase difference at the connection points. The inner ring is connected to the waveguide body. By selecting the ring radius to match the OAM order (q), as specified above, and following the field mode analysis in [16] it can be shown that only TE_{nm} modes with an n -index matching the OAM order ($n = q$) are allowed to propagate. Moreover, by appropriate selection of the waveguide radius, it is possible to cut off any

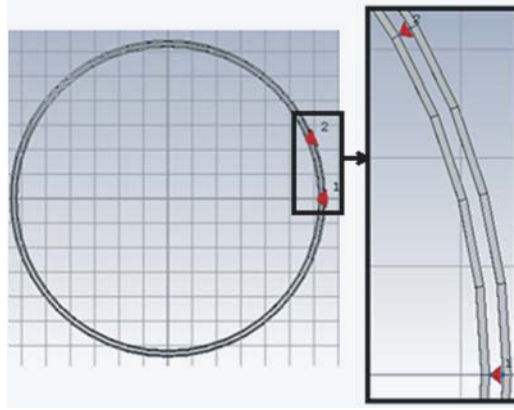


Figure 1. Two-ring feeders used to generate a traveling wave of order 4. The average radius of the rings is 3.2 mm. Inset to the right shows two excitation ports with 22.5° separation. The rings are separated by 0.4 mm (8%λ at an operating frequency of 60 GHz).

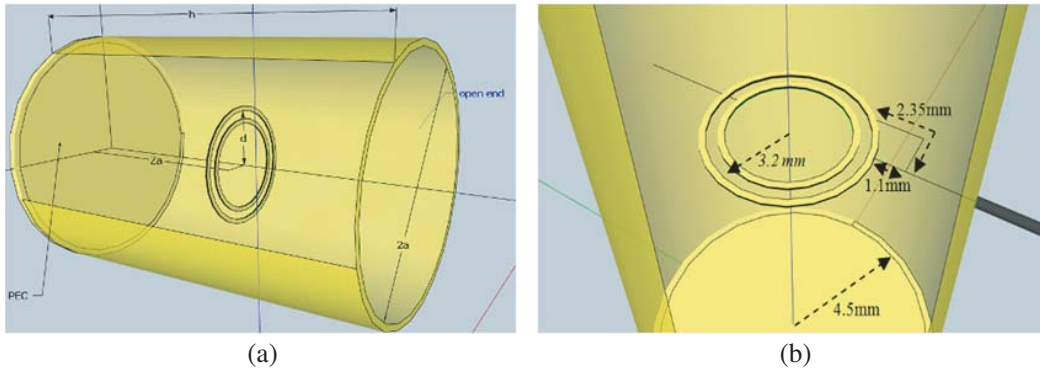


Figure 2. (a) General schematic of the waveguide structure. (b) Rings feeding and grounding.

TM mode having the same n -index (and therefore having the same azimuthal characteristics) of the propagating TE mode. This prevents distortions in the phase spatial distribution.

3. FIELD DERIVATION

Considering TE to the z -direction, the electric vector potential F should be z -directed [22, 23] and satisfy the equation

$$\nabla^2 F_z + K^2 F_z = -\varepsilon M, \tag{1}$$

where ∇^2 is the Laplacian operator, and ε is the medium permittivity. The magnetic current density M , and consequently the solution of F_z , depends on the distribution of the current flow in the feeding ring. To excite the required traveling-wave for generating the q -th OAM order the current should have a density modeled by the spatial distribution

$$J = J_o \frac{\delta(\rho - d)}{\rho} \delta(z - z_a) e^{jq\theta} \hat{\theta}. \tag{2}$$

In this model the ring is assumed thin enough to be sufficiently represented by Dirac-delta function $\delta(\cdot)$, $\hat{\theta}$ is a unit direction, and J_o is an amplitude factor. Using cylindrical coordinates, a solution to Eq. (1) takes the general product form

$$F_z = e^{jq\theta} f(\rho) g(z). \tag{3}$$

Because of the delta inhomogeneous term in Eq. (2), the form of the radial-dependent term $f(\rho)$ is different in $\rho < d$ and $\rho > d$ regions

$$f(\rho) = \begin{cases} B_1 J_q(\eta\rho) & 0 < \rho < d \\ C_1 J_q(\eta\rho) + C_2 Y_q(\eta\rho) & d < \rho < a \end{cases}, \quad (4)$$

where $Y_q(\cdot)$ is the q -th-order Neumann function. Similar reasoning applies to the z -dependent term $g(z)$ which can be written as

$$g(z) = \begin{cases} A_1 \sin(\mathcal{L}z) & 0 < z < z_a \\ A_2 e^{j\mathcal{L}z} & z_a < z < h \end{cases}. \quad (5)$$

Constants B_1 , C_1 , C_2 , A_1 , and A_2 in Eqs. (4) and (5) are to be determined from boundary and excitation conditions. The electric field azimuthal component is available as

$$E_\emptyset = \frac{1}{\varepsilon} \frac{dF_z}{d\rho} = \frac{\eta}{\varepsilon} e^{jq\emptyset} g(z) \begin{cases} B_1 \dot{J}_q(\eta\rho) & 0 < \rho < d \\ C_1 \dot{J}_q(\eta\rho) + C_2 \dot{Y}_q(\eta\rho) & d < \rho < a \end{cases},$$

where prime indicates derivation with respect to ρ . Imposing boundary conditions at the sidewalls of the waveguide ($\rho = a$) the field expression becomes

$$E_\emptyset = \frac{\eta}{\varepsilon} e^{jq\emptyset} g(z) \begin{cases} B_1 \dot{J}_q(\eta\rho) & 0 < \rho < d \\ B_2 \left[\dot{J}_q(\eta a) \dot{Y}_q(\eta\rho) - \dot{J}_q(\eta\rho) \dot{Y}_q(\eta a) \right] & d < \rho < a \end{cases},$$

with B_2 being a constant. Continuity of E_\emptyset at the sides of the thin ring implies the following relations

$$B_1 = B_2 \frac{1}{\dot{J}_q(\eta d)} \left[\dot{J}_q(\eta a) \dot{Y}_q(\eta d) - \dot{J}_q(\eta d) \dot{Y}_q(\eta a) \right] \quad (6a)$$

$$A_1 = A_2 \frac{e^{j\mathcal{L}z_a}}{\sin(\mathcal{L}z_a)} \quad (6b)$$

An excitation condition is formed by the aid of Ampere's law in the \emptyset -direction

$$\frac{\partial H_\rho}{\partial z} - \frac{\partial H_z}{\partial \rho} - j\omega\varepsilon E_\emptyset = J, \quad (7)$$

where H_ρ and H_z are, respectively, the ρ and z -components of the magnetic field, which follow directly from Maxwell's equations as

$$H_\rho = \frac{-j}{\omega\mu\varepsilon} e^{jq\emptyset} \frac{\partial g(z)}{\partial z} \frac{\partial f(\rho)}{\partial \rho}$$

$$H_z = \frac{-j}{\omega\mu\varepsilon} \eta^2 e^{jq\emptyset} g(z) f(\rho),$$

where μ is the medium permeability. Noting the radial continuity of both E_\emptyset and H_ρ across $\rho = d$ the Left-Hand Side (LHS) of Eq. (7) leads after integration across $\rho = d$ in the region $0 < z < z_a$ to

$$-\lim_{\epsilon \rightarrow 0} H_z]_{d-\epsilon}^{d+\epsilon} = \frac{j}{\omega\mu\varepsilon} \eta^2 e^{jq\emptyset} A_1 \sin(\mathcal{L}z) \left\{ B_2 \left[\dot{J}_q(\eta a) Y_q(\eta d) - J_q(\eta d) \dot{Y}_q(\eta a) \right] - B_1 J_q(\eta d) \right\},$$

which can be simplified using Eq. (6a) and Wronskian identity

$$J_q(\eta d) \dot{Y}_q(\eta d) - \dot{J}_q(\eta d) Y_q(\eta d) = \frac{2}{\pi \eta d},$$

to

$$\frac{-2\eta j}{\omega\mu\varepsilon \pi d} e^{jq\emptyset} A_1 B_2 \sin(\mathcal{L}z) \frac{\dot{J}_q(\eta a)}{\dot{J}_q(\eta d)}.$$

The Right-Hand Side (RHS) of Eq. (7) after integration across $\rho = d$ produces

$$\frac{J_o}{d} e^{jq\emptyset} \delta(z - z_a).$$

Both forms extracted from the LHS and RHS of Eq. (7) are then multiplied by $\sin(\mathcal{L}z)$ and integrated over an appropriate period of z to yield

$$A_1 B_2 = \frac{j\omega\mu\varepsilon}{2\eta} J_o \sin(\mathcal{L}z_a) \frac{\dot{J}_q(\eta d)}{\dot{J}_q(\eta a)}$$

from which the field expression in $0 < z < z_a$ becomes

$$E_\theta = j\omega\mu \frac{J_o}{2} \sin(\mathcal{L}z_a) \sin(\mathcal{L}z) e^{jq\theta} \begin{cases} \frac{\dot{J}_q(\eta\rho)}{\dot{J}_q(\eta a)} \left[\dot{J}_q(\eta a) \dot{Y}_q(\eta d) - \dot{J}_q(\eta d) \dot{Y}_q(\eta a) \right] & 0 < \rho < d \\ \frac{\dot{J}_q(\eta d)}{\dot{J}_q(\eta a)} \left[\dot{J}_q(\eta a) \dot{Y}_q(\eta\rho) - \dot{J}_q(\eta\rho) \dot{Y}_q(\eta a) \right] & d < \rho < a \end{cases}. \quad (8)$$

A similar solution can be written for the field in the $z_a < z < h$ region, mainly the base $\sin(\mathcal{L}z)$ has to be replaced by $e^{j\mathcal{L}z}$ to indicate an outgoing wave. The field component E_θ is used in the next section to formulate the input impedance.

4. INPUT IMPEDANCE

In this section, the input impedance of the model is derived. Using the complex Poynting vector theorem [24], it is possible to define the input impedance in reference to the ring's input current I by

$$Z_{in} = \frac{-1}{I^2} \int_{\bar{v}} E_\theta J^* d\bar{v},$$

where \bar{v} represents the ring dimensions, and the superscript $*$ stands for complex conjugation. Noting that $\omega\mu = Z_o K_o$, with Z_o being the free-space impedance, a simplified expression can be obtained:

$$Z_{in} = -jZ_o K_o \pi d \sin^2(\mathcal{L}z_a) \frac{\dot{J}_q(\eta d)}{\dot{J}_q(\eta a)} \left[\dot{J}_q(\eta a) \dot{Y}_q(\eta d) - \dot{J}_q(\eta d) \dot{Y}_q(\eta a) \right]. \quad (9)$$

The general form of this expression is similar to that obtained in [10]. The poles of these expressions are determined by the zeros of the Bessel function derivative. We shall denote the m -th zeros of $\dot{J}_q(\cdot)$ and $J_q(\cdot)$ as $\dot{p}_{q,m}$ and $p_{q,m}$, respectively. The pole location points to a resonance location at which the real part of the input impedance rises to a large positive value and the imaginary part approaches zero. A typical impedance spectrum includes a main resonance in addition to side resonances. The total spectrum over all resonances is obtained by adding Eq. (9) at the different poles.

It is also noted from Eq. (9) that Z_{in} depends on z_a , which is the ring location corresponding to the short-circuit (PEC) terminal. Thus, this value can be controlled to enable maximum power transfer from the coaxial line feed. The effect of parameter z_a on resonance is shown later in Fig. 4.

5. DISPERSION ANALYSIS

The transverse wave number at resonance can be found through the transverse resonance technique. This technique has been applied in [10] and [11] to a closed cylindrical waveguide structure. Similar steps are followed in the analysis here. The cross section of the waveguide along the z -axis is represented by a Transmission Line (TL) of length h for which the resonance condition inside the waveguide at a distance l from the PEC terminal is

$$\frac{1}{Z_{tp}} + \frac{1}{jZ_g \tan(\mathcal{L}l)} = 0, \quad (10)$$

where $Z_g = K_o Z_o / \mathcal{L}$ is the TL characteristic impedance in TE mode. The denominator of the second term in Eq. (10) is the result of transforming the short-circuit impedance of the PEC terminal a distance l . In the first term of Eq. (10), Z_{tp} is the transformation of Z_p a distance $(h-l)$ inside the waveguide away from its open end, that is

$$Z_{tp} = \frac{Z_g (Z_p + jZ_g \tan(\mathcal{L}(h-l)))}{Z_g + jZ_p \tan(\mathcal{L}(h-l))}.$$

where Z_p combines the effect of the medium outside the waveguide [13] and the aperture reactance (in case a sheet is installed).

The resonance condition in Eq. (10) can be reformulated [24] using a first-order approximation of $\tan(\mathcal{L}l)$ as

$$\frac{1}{Z_{tp}} + \frac{1}{jZ_g(\mathcal{L}l - n\pi)} = 0 \quad \text{for } n=0, 1, 2, \dots \quad (11)$$

Dispersion curves are plots of the solutions of Eq. (11) for the real and imaginary parts of η , which are denoted β and α , respectively. Typical dispersion curves are depicted in Fig. 3 for different values of l , where for the sake of simplicity β and α are normalized by K_o . Clearly, these curves vary from point to point along the axial direction. Accordingly, the axial location of a feeding ring inside the waveguide affects its input impedance. This effect is expected to be notable for large rings [25]. The analysis carried out so far is applied in the next section to predict the locations of resonances in the impedance spectrum.

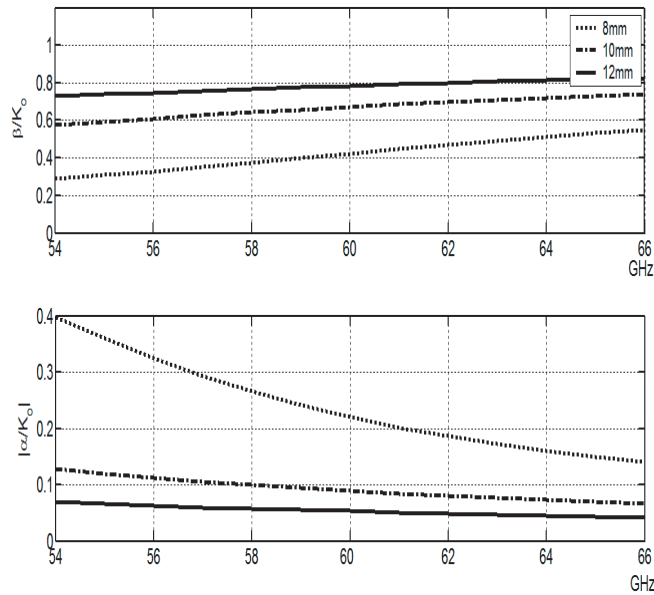


Figure 3. Dispersion curves at different axial distances: $l = 8, 10,$ and 12 mm. The waveguide radius is 3.5 mm and length is 20 mm. Results are shown for an index $n = 3$ in Eq. (11).

6. DISPERSION RELATION AND INPUT IMPEDANCE SPECTRUM

The resonance spectrum depends on the location of the feeding ring and the size of the waveguide structure. Observations are made in Fig. 4 using CST and are used as base for the next analysis. Fig. 4(a) shows that the input impedance is almost unaffected by the change in the waveguide length. In this part of the figure the waveguide radius (a) and the distance (z_a) between the ring and the PEC terminal are not changed. Only the distance between the ring and the open end of the waveguide is increased. The result in Fig. 4(a) is expected for the absence of the backward traveling wave which could alter the input impedance. The forward traveling wave formed in the region above the ring keeps its way toward the waveguide open end. The picture is different in Fig. 4(b) when the waveguide length is fixed but its radius and z_a are changed. It is notable that the resonances shift to the right as the waveguide radius decreases.

The previous observations and the spectrum in general can be better understood through dispersion analysis as follows:

- Dispersion curves from Eq. (11) are plotted for different values of n in Fig. 5, where the curves are evaluated at the ring location inside the waveguide, i.e., at $l = z_a$.

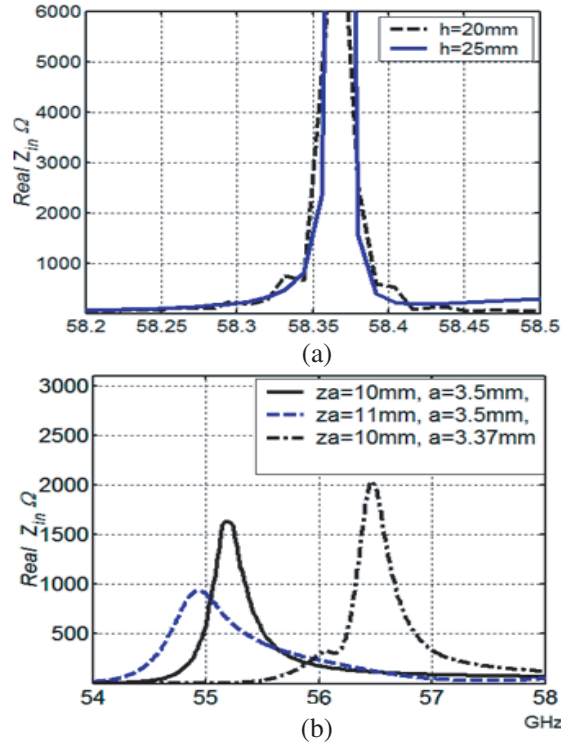


Figure 4. Input impedance for different (a) waveguide lengths and (b) feeding ring locations and waveguide radii.

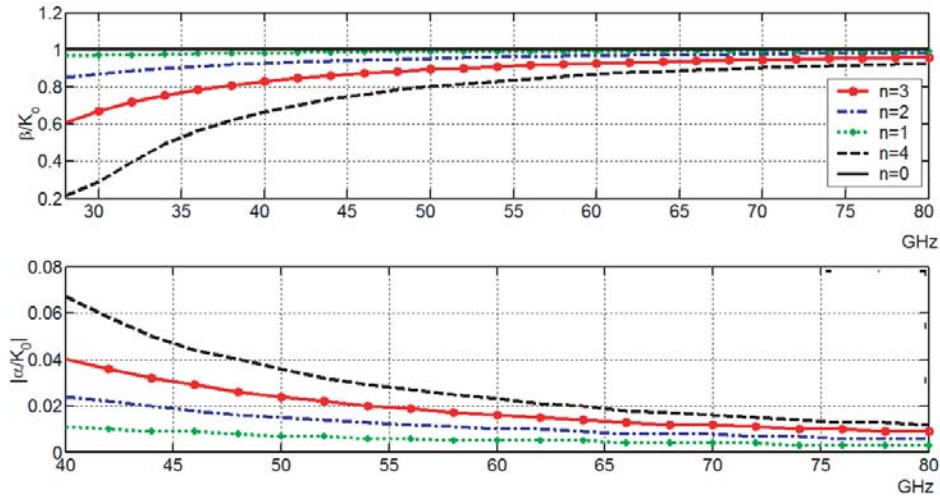


Figure 5. Dispersion curves evaluated for different values of n . Waveguide of 3.5 mm radius and 20 mm length is considered.

- The zeros of the Bessel-derivative function in the denominator of the impedance formula in Eq. (9) are poles of the expression and are therefore pointing to the locations of the resonances.
- The locations of the resonances are specified by the intersections of the dispersion curves with those curves representing the zeros of the Bessel-derivative. The latter curves are given, after normalization via K_o , by

$$\frac{\beta}{K_o} = \frac{\dot{p}_{q,m}}{aK_o} \quad \text{for } m = 1, 2, \dots \quad (12)$$

- It is noted in Fig. 5 that the dispersion curves with smaller values of n converges faster. As the curves from Eq. (12) are descending in frequency they will first intersect the dispersion curve with the smallest value of n ($n = 0$ in the upper part of Fig. 5). This defines the main resonance location. The intersection with the dispersion curve corresponding to the next value of n should define the first side-resonance, and so on.

Numerical examples demonstrating how to determine the resonances from these curves intersections are given in the results section. Regarding the main resonance, since the dispersion curve with $n = 0$ converges rapidly, the intersection is likely to occur at $\beta/K_o = 1$. This likelihood corresponds with the fact that traveling-wave radiation occurs at $\beta/K_o = 1$ for a finite aperture [26]. Simulations show, however, a small shift in the resonance from its expected value to a lower frequency. This shift is caused by the influence of the waveguide structure on the spectrum of the ring radiator. This frequency shift corresponds to a value of β/K_o slightly larger than one, as shown in Table 1.

Table 1. Resonances found from CST simulations and the corresponding η/K_o for ring of 2.4 mm average radius placed at different locations inside a waveguide of 3.5 mm radius and 20 mm length.

z_a (mm)	Main resonance		1st side resonance		2nd side resonance	
	(GHz)	η/K_o	(GHz)	η/K_o	(GHz)	η/K_o
9	55.3	$1.036 - j0.20$	60.1	$0.95 - j0.11$	66.0	$0.84 - j0.80$
12	55.47	$1.033 - j0.07$	58.8	$0.97 - j0.05$	62.8	$0.91 - j0.04$

From Table 1, it is also possible to compare the normalized attenuation constants (α/K_o) of the main and side resonances. The presence of an attenuation constant, even though the structure is lossless, shows power leakage in the form of radiation from the open end of the waveguide [27]. The high value of α indicates high radiation and beam width at the main resonance.

7. RESULTS

Results are presented to demonstrate the previous ideas. We begin by generating a traveling wave from a superposition of two standing waves. Then, field distributions are demonstrated inside and outside the waveguide. Also, the derived input impedance formula is compared against full-wave numerical simulation. Finally, the spectrum resonances are detected using the curve intersection method.

7.1. Traveling Wave Generation Using Two-Ring Feeder

Figure 6 shows the far field radiation pattern and the field intensity resulting from the two-ring configuration in Fig. 1. The average radius of the rings needed to generate a 4th order OAM is 3.2 mm. The standing wave patterns of the individual sources appear in the upper two rows of Fig. 6. It appears that the null of one source matches a peak of the other source. This leads to an approximately constant far field pattern for the superposition as shown in the lower row of the figure. The traveling wave is well known [28] to have a far field of constant amplitude in the transverse plane. Some ripple appears in the field pattern, this attributes to the separation left between the inner and outer rings.

7.2. Field Distribution Inside the Waveguide

Field distributions based on Eq. (8) are simulated in Fig. 7 for a 20 mm-long airfield waveguide at 60 GHz. A TE mode is generated inside the waveguide at certain OAM order by carefully selecting the waveguide radius. For instance, for the third OAM order a waveguide of radius in the range $\hat{p}_{31}/K_o < a < p_{31}/K_o$ would pass the TE_{31} mode and prevent the TM_{31} mode. In the simulation, $a = 3.5$ mm is used. For OAM orders 2 and 4, radii of 2.5 mm and 4.5 mm are respectively used to prevent the TM_{21} and TM_{41} modes. The ring circumference at the specified frequency should be $5q$ mm. For this purpose, rings of average radii 1.6 mm, 2.4 mm, and 3.2 mm are used with OAM orders 2, 3, and 4, respectively. As shown

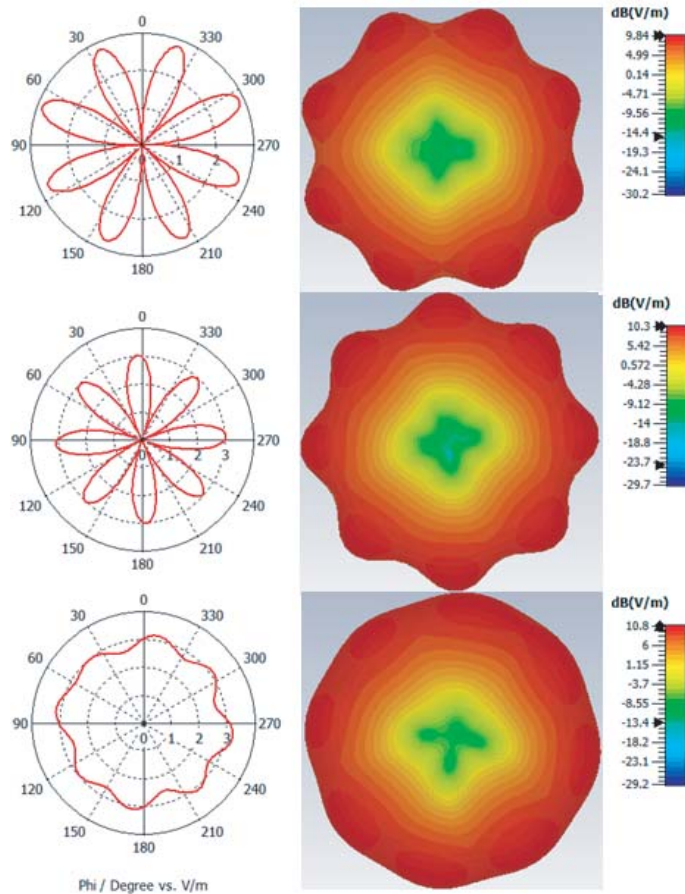


Figure 6. CST results for generating OAM wave of order 4 using the two rings method. Shown are the far field patterns (left column) and field intensities (right column) for the individual sources (two upper rows) and the superposition (lower row).

in Fig. 7, a change in the amplitude colour from blue to red indicates an increase in the field value. The deep blue at the centre indicates a null. The null apparently increases by increasing the OAM order. Also, the amplitude vanishes at the waveguide sidewalls in response to the boundary conditions. The field phase distribution for each of the shown cases exhibits for one rotation around the waveguide axis a complete change of 2π radians for a number of times equaling the OAM order.

7.3. Field Propagation Outside the Waveguide

Propagation properties of the vortex beam outside the open end of the waveguide are shown in this subsection. Used formulas are given in the Appendix. The waveguide settings are the same as in the previous subsection. Figs. 8 and 9 show the distributions of the magnetic field z -component (H_z) for OAM orders 2 and 4, respectively. Results are demonstrated over a square observation window in the transverse plane at different distances from the open end of the waveguide. The field amplitude exhibits a ring-like form and the rings expand at propagation. This expansion, an inherent property of OAM carrying waves, is further explained by tracking two rings of intensities (marked 1 and 2 in Fig. 8) and noting how the sizes of these rings expanded between Fig. 8(a) (at $z = 5$ mm) and Fig. 8(b) (at $z = 30$ mm). Also, by comparing Fig. 8 (OAM order 2) to Fig. 9 (OAM order 4) one notes that suchbeam expansion is more obvious at the larger OAM orders. The phase of the field shows clockwise helical distribution. Clockwise rotation is the convention followed here for positive OAM orders. At any point in the observation window the phase takes a value of $q\theta$. The field phase and amplitude distributions are in agreement with those predicted theoretically for a vortex beam.

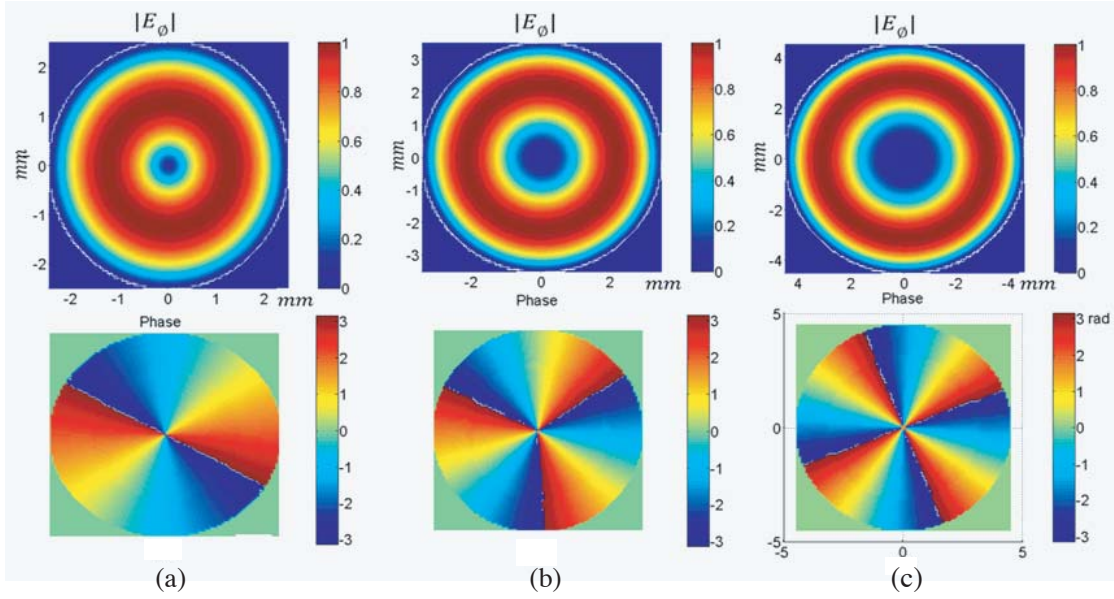


Figure 7. Normalized amplitude (upper row) and phase (lower row) distributions of E_θ inside the waveguide for (a) OAM = 2, (b) OAM = 3, and (c) OAM = 4.

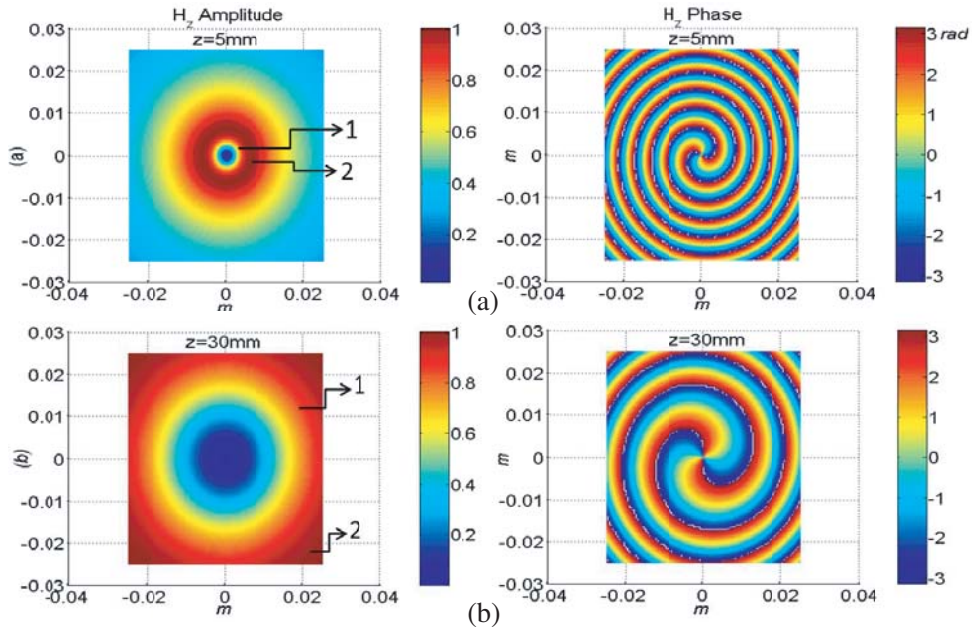


Figure 8. H_z -field (normalized) distribution for a beam with OAM order $q = 2$ over a $25 \times 25 \text{ mm}^2$ area located at (a) 5 mm, and (b) 30 mm from the transmitting aperture.

7.4. Input Impedance Spectrum

In this subsection, the input impedance based on Eq. (9) is compared against the result obtained via CST simulations. The input impedance is considered for a waveguide of 3.37 mm radius and 20 mm length. The third OAM order is used in this simulation and the excitation rings are placed at $z_a = 12 \text{ mm}$. Results are shown in Fig. 10. The main resonance appears at 57.242 GHz. CST simulation and the formula results match very well. The transverse propagation wavenumber used in Eq. (9) is $\eta = (1.036 - j0.005)K_o$.

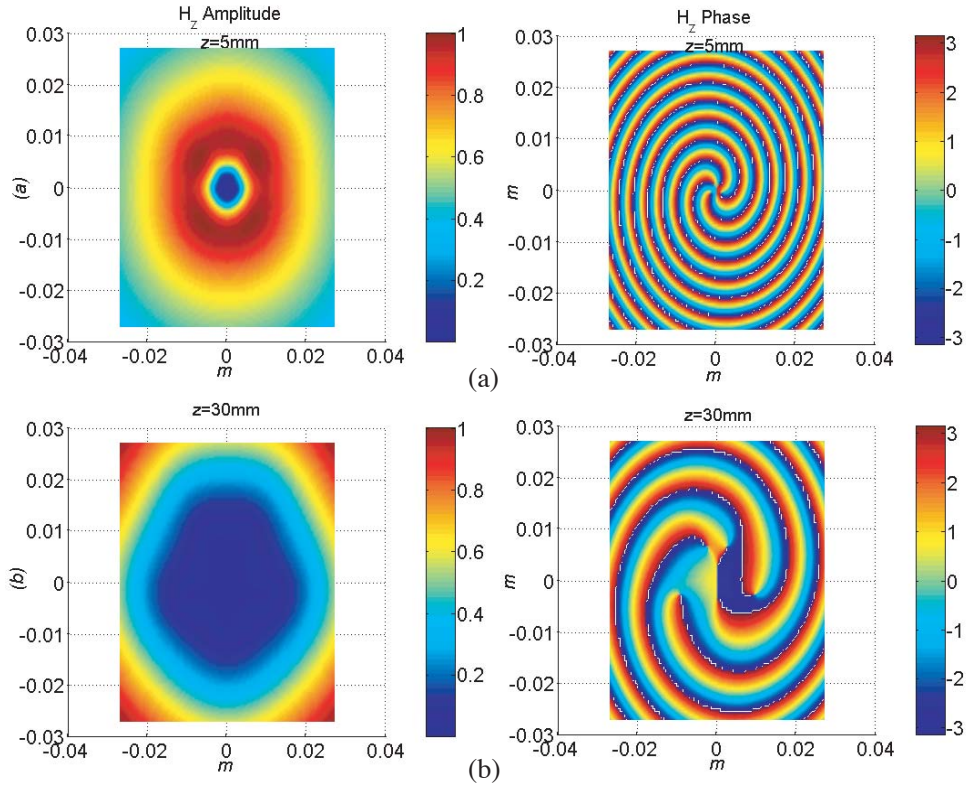


Figure 9. H_z -field (normalized) distribution for a beam with OAM order $q = 4$ over a $25 \times 25 \text{ mm}^2$ area located at (a) 5 mm, and (b) 30 mm from the transmitting aperture.

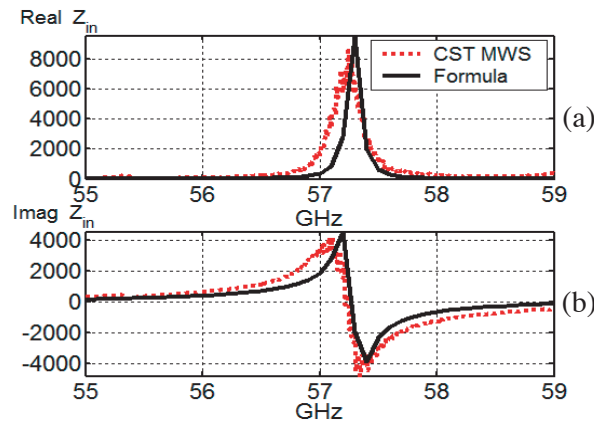


Figure 10. (a) Real and (b) imaginary of the input impedance at main resonance as obtained by Eq. (9) and confirmed by CST simulation.

Resonance frequencies and the corresponding values of η can be obtained from the dispersion curves. To demonstrate this point, real-normalized dispersion curves (β/K_o) are plotted in the upper part of Fig. 11 for different values of n . These curves are obtained using Eq. (11) at $l = 12 \text{ mm}$, i.e., at the ring location. In the upper part of Fig. 11 also appears the normalized Bessel-derivative zero curve from Eq. (12) (the dotted descending curve). The intersections of this curve with the dispersion curves should determine the locations of the resonances. The impedance spectrum as obtained by CST is shown in the lower part of Fig. 11, where the resonances can be noted. By comparing the lower and upper parts of Fig. 11, it is obvious that the side-resonances at 60.6 GHz and 64.5 GHz in the impedance

spectrum match the intersections in the dispersion curve. At the first side-resonance, the normalized Bessel-derivative zero curve crosses the $n = 1$ dispersion curve at 60.6 GHz, then it crosses the $n = 2$ dispersion curve at 64.5 GHz to indicate the second side-resonance location.

Another case is studied in Fig. 12 for a waveguide of radius 3.37 mm and length of 20 mm. The excitation ring average radius is 2.4 mm which corresponds to OAM order 3. The ring is placed at $z_a = 18$ mm. Three side resonances appear besides the main resonance in the range from 54 GHz to 66 GHz. The side resonances are determined in Fig. 12 with good accuracy up to a maximum error of $\Delta_2 < 0.3\%$.

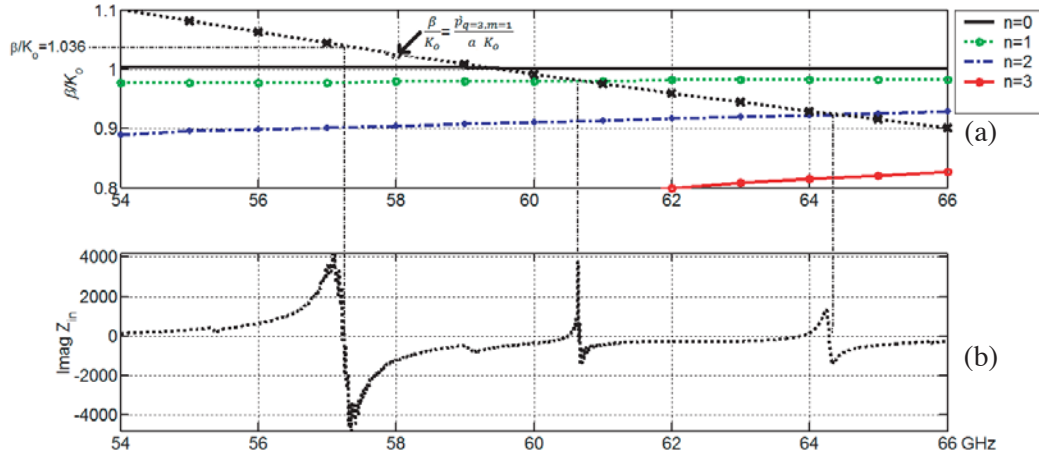


Figure 11. (a) Dispersion curves and (b) input impedance spectrum obtained by CST. In the upper part also appears the normalized Bessel-derivative curve. Comparing both parts of the figure shows a good match between the resonances and the curves intersections in the upper part.

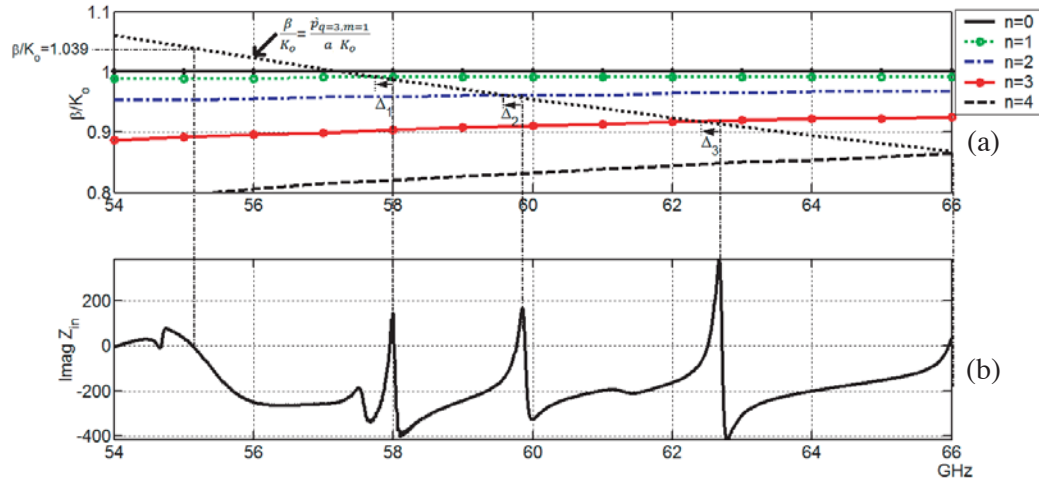


Figure 12. Dispersion curves for (a) $z_a = 18$ mm and (b) the input impedance spectrum.

The last part of the numerical results is dedicated to some of the observations made in Fig. 5. A shift to the right in resonances is observed in Fig. 5(b) when the waveguide radius is changed from 3.5 mm to 3.37 mm. This shift is traced in Fig. 13. The normalized Bessel-derivative zero curve shifts up as the waveguide radius decreases while the dispersion curves remain unchanged because the waveguide length is not changed. This moves the points of the curves intersections in the upper part of Fig. 13 to the right as noted in the figure.

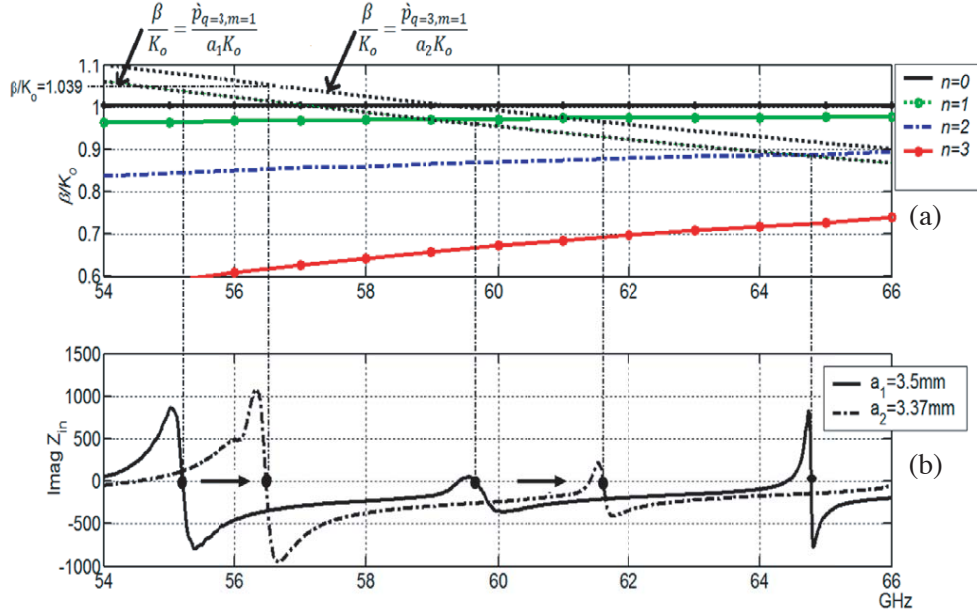


Figure 13. (a) Dispersion curves and (b) input impedance spectrum for a 20 mm waveguide. Resonances witness shift to the right as the waveguide radius is changed from $a_1 = 35$ mm to $a_2 = 337$ mm.

8. CONCLUSIONS

This paper proposed vortex beam generation using a simple feeder of two rings. The configuration was set up to provide traveling wave excitation at certain OAM order by the superposition of two standing waves. The feeder was placed in an open-ended cylindrical waveguide to focus and direct the radiation. Simulations verified the conclusions drawn in the theoretical derivation: a propagating vortex beam was generated; the field phase and amplitude distributions were in agreement with those predicted theoretically for a vortex beam.

The system model was derived, and a detailed dispersion analysis was done to predict the spectrum resonances. The analysis was also used as a base to explain some changes that happen on the locations of the resonances for various configurations. Accurate predictions were shown based on certain intersections of curves in the dispersion plots. The resonances were determined at broadband spectra. The error of predicting the resonance location was less than 0.3%.

As a future work, we consider applying the proposed method for more than one ring to create a superposition of OAM orders to be used in beam forming.

APPENDIX A.

In this appendix, we show the basic formulas used to obtain the results for calculating the magnetic field outside the waveguide. According to the electromagnetic equivalence principle [22], the magnetic field radiated by an aperture can be considered equivalently as radiation caused by surface electric currents flowing over the aperture. For the z -field component, we have

$$H_z = \frac{-1}{4\pi} \int_{\hat{s}} (R \times J^a)_z \frac{1 + i\mathcal{L}R}{|R|^3} e^{-i\mathcal{L}R} d\hat{s},$$

where \hat{s} is the surface of the aperture, and R denotes the distance between a point located on the aperture $(\hat{\rho}, \hat{\theta}, h)$ and an observation point (ρ, θ, z) at which the field is to be evaluated. The aperture surface current J^a in terms of the aperture magnetic field is

$$J^a = 2\hat{z} \times H^a = 2H_\rho^a \hat{\theta} - 2H_\theta^a \hat{\rho},$$

with $H_\rho^a = \frac{-j}{w\mu\epsilon} \frac{\partial^2 F_z}{\partial \rho \partial z} \Big|_{z=h}$, and $H_\theta^a = \frac{-j}{w\mu\epsilon\rho} \frac{\partial^2 F_z}{\partial \theta \partial z} \Big|_{z=h}$, where F_z is given by Eq. (3).

REFERENCES

1. Poynting, J. H., "The wave motion of a revolving shaft, and a suggestion as to the angular momentum in a beam of circularly polarised light," *Proceedings of the Royal Society of London. Series A, Containing Papers of a Mathematical and Physical Character*, Vol. 82, No. 557, 560–567, 1909.
2. Beth, R. A., "Mechanical detection and measurement of the angular momentum of light," *Physical Review*, Vol. 50, No. 2, 115–125, 1936.
3. Allen, L., M. W. Beijersbergen, R. J. Spreeuw, and J. P. Woerdman, "Orbital angular-momentum of light and the transformation of Laguerre-Gaussian laser modes," *Physical Review A*, Vol. 45, No. 11, 8185–8189, 1992.
4. Chen, R., Member, H. Zhou, M. Moretti, X. Wang, and J. Li, "Orbital angular momentum waves: generation, detection and emerging applications," arXiv preprint arXiv:1903.07818, Mar. 2019.
5. Thidé, B., H. Then, J. Sjöholm, K. Palmer, J. Bergman, T. D. Carozzi, Y. N. Istomin, N. H. Ibragimov, and R. Khamitova, "Utilization of photon orbital angular momentum in the low-frequency radio domain," *Physical Review Letters*, Vol. 99, No. 8, 087701-1–087701-4, Aug. 2007.
6. Durnin, J. J. J. M., J. J. Miceli Jr, and J. H. Eberly, "Diffraction-free beams," *Physical Review Letters*, Vol. 58, No. 15, 1499–1501, Apr. 1987.
7. Barbuto, M., F. Trotta, F. Bilotti, and A. Toscano, "Circular polarized patch antenna generating orbital angular momentum," *Progress In Electromagnetics Research*, Vol. 148, 23–30, 2014.
8. Huang, M., X. Zong, and Z. P. Nie, "Horn antenna generating electromagnetic field with orbital angular momentum," *Progress In Electromagnetics Research M*, Vol. 60, 57–65, 2017.
9. Al-Bassam, A., M. A. Salem, and C. Caloz, "Vortex beam generation using circular leaky-wave antenna," *IEEE Antennas and Propagation Society International Symposium (APSURSI)*, 1792–1793, 2014.
10. Ettorre, M. and A. Grbic, "Generation of propagating Bessel beams using leaky-wave modes," *IEEE Transactions on Antennas and Propagation*, Vol. 60, No. 8, 3605–3613, 2012.
11. Lu, P., D. Voyer, A. Bréard, J. Huillery, B. Allard, X. Lin-Shi, and X. S. Yang, "Design of TE-polarized bessel antenna in microwave range using leaky-wave modes," *IEEE Transactions on Antennas and Propagation*, Vol. 66, No. 1, 32–41, 2018.
12. Dheyab, E. and N. Qasem, "Design and optimization of rectangular microstrip patch array antenna using frequency selective surfaces for 60 GHz," *International Journal of Applied Engineering Research*, Vol. 11, No. 7, 4679–4687, 2016.
13. Pelin, N., M. H. Salem, E. Niver, and M. A. Salem, "Microwave vortex beam launcher design," *IET Journal on Microwaves, Antennas & Propagation*, Vol. 12, No. 14, 2149–2153, 2018.
14. Mao, F., T. Li, Y. Shao, J. Yang, and M. Huang, "Orbital angular momentum radiation from circular patches," *Progress In Electromagnetics Research Letters*, Vol. 61, 13–18, 2016.
15. Hui, X., S. Zheng, Y. Chen, Y. Hu, X. Jin, H. Chi, and X. Zhang, "Multiplexed millimeter wave communication with dual orbital angular momentum (OAM) mode antennas," *Scientific Reports*, Vol. 5, No. 1, 1–9, 2015.
16. Berglind, E. and G. Bjork, "Humblet's decomposition of the electromagnetic angular moment in metallic waveguides," *IEEE Transactions on Microwave Theory and Techniques*, Vol. 62, No. 4, 779–788, 2014.
17. Alamayreh, A., N. Qasem, and J. Rahhal, "General configuration MIMO system with arbitrary OAM," *Electromagnetics*, Vol. 40, No. 5, 343–353, 2020.
18. Cheng, W., H. Zhang, L. Liang, H. Jing, and Z. Li, "Orbital-angular-momentum embedded massive MIMO: Achieving multiplicative spectrum-efficiency for mmWave communications," *IEEE Access*, Vol. 6, 2732–2745, 2017.

19. Zheng, S., Y. Chen, Z. Zhang, X. Jin, H. Chi, X. Zhang, and Z. N. Chen, "Realization of beam steering based on plane spiral orbital angular momentum wave," *IEEE Transactions on Antennas and Propagation*, Vol. 66, No. 3, 1352–1358, 2017.
20. Cheng, W., W. Zhang, H. Jing, S. Gao, and H. Zhang, "Orbital angular momentum for wireless communications," *IEEE Wireless Communications*, Vol. 26, No. 1, 100–107, 2018.
21. Astley, V., B. McCracken, R. Mendis, and D. M. Mittleman, "Analysis of rectangular resonant cavities in terahertz parallel-plate waveguides," *Optics Letters*, Vol. 36, No. 8, 1452–1454, 2011.
22. Balanis, C. A., *Advanced Engineering Electromagnetic*, John Wiley & Sons, New York, 1989.
23. Collin, R. E., *Foundations for Microwave Engineering*, McGraw-Hill, New York, 1966.
24. Fuscaldo, W., G. Valerio, A. Galli, R. Sauleau, A. Grbic, and M. Ettorre, "Higher-order leaky-mode bessel-beam launcher," *IEEE Transactions on Antennas and Propagation*, Vol. 64, No. 3, 904–913, 2015.
25. King, R. W. P., "The loop antenna for transmission and reception," *Antenna Theory, Part 1*, 1st Edition, Inter-University Electronic Series, Vol. 7, Chap. 11, 458–482, R. E. Collin and F. J. Zucker, ed., McGraw-Hill, New York, 1969.
26. Sutinjo, A., M. Okoniewski, and R. H. Johnston, "Radiation from fast and slow traveling waves," *IEEE Antennas and Propagation Magazine*, Vol. 50, No. 4, 175–181, 2008.
27. Jackson, D. R. and A. A. Oliner, "Leaky-wave antennas," *Modern Antenna Handbook*, Chap. 7, 325–367, C. Balanis, ed., Wiley, New York, NY, USA, 2008.
28. Knudsen, H. L., "The field radiated by a ring quasi-array of an infinite number of tangential or radial dipoles," *Proceedings of the IRE*, Vol. 41, No. 6, 781–789, 1953.